Neuromorphic Tactile Sensing System for Textural Features Classification

Haydar Al Haj Ali, Yahya Abbass, *Member, IEEE*, Christian Gianoglio, *Member, IEEE*, Ali Ibrahim, *Member, IEEE*, Changjae Oh, *Member, IEEE*, and Maurizio Valle, *Senior Member, IEEE*

***Abstract*—Artificial tactile sensing systems have gained significant attention in recent years due to their potential to enhance human–machine interaction. Numerous initiatives have been introduced to shift the computational paradigms of these systems toward a more biologically inspired approach, by incorporating neuromorphic computing methods. Despite the significant advances made by these systems, dependence on complex offline methods for classification (i.e., hand-crafted encoding features) remains a limitation for their real-time deployment. In this work, we present a neuromorphic tactile P(VDF-TrFE) poly(vinylidene fluoride trifluoroethylene)-based (PVDF) sensing system for textural features classification, that employs raw signals directly for classification. We first converted raw signals into spikes and then trained recurrent spiking neural networks (RSNNs) using backpropagation through time (BPTT) with surrogate gradients to perform classification. We proposed an optimization method based on tuning the refractory period of the encoding neurons, to explore a potential trade-off between the computational cost and the classification accuracy of the RSNN. The proposed method effectively identified two RSNNs with refractory period configurations that achieved a trade-off between the two evaluation metrics. Following this, we reduced the inference time steps of the selected RSNN during inference using a rate-coding-based method. This method succeeded in saving around 26.6% out of the total original time steps. In summary, the proposed system paves the way for establishing an end-to-end neuromorphic approach for tactile textural features classification, by deploying the selected RSNNs on a dedicated neuromorphic hardware device for real-time inferences.**

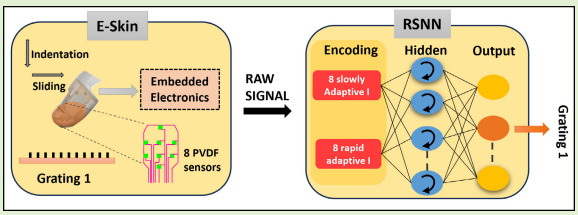

***Index Terms*— Gratings, recurrent spiking neural network (RSNN), refractory period, spatiotemporal, tactile sensing system, textural features.**

I. Introduction

A. Motivation

HUMAN skin, with its vast network of sensory receptors, serves as the primary interface with the external world, enabling it to perceive and interpret a diverse range of tactile sensations. The perception of touch, which is delivered by the skin, relies on four types of mechanoreceptors innervating the glabrous skin, namely: Merkel cells (SA-I), Ruffini ending (SA-II), Meissner (RA-I), and Pacinian's (RA-II) corpuscles [1]. These mechanoreceptors, synergistically, contribute to the somatosensory system in serving the exteroceptive and interoceptive functions [2].Drawing inspiration from the sophistication of human skin, artificial tactile sensing systems have emerged, aiming to replicate the skin's physiological features, using a variety of methods (i.e., complex electronics, data processing, and sophisticated materials). These systems have important applications in prosthetics [3], [4] and robotics [5]. This electronic skin (e-skin) endows the robots with cutting-edge abilities to augment interaction with their surroundings such as perceiving texture [6], stiffness [7], and shape [8], [9]. Tremendous efforts have been made to establish an adequate artificial replication of the human skin behavior [10], [11], [12]. These endeavors include: 1) exploring a wide range of materials used for sensor fabrication to cover the mechanoreceptors' frequency bandwidth (1 Hz–1 kHz) [11]; 2) developing algorithms to process tactile information efficiently [12] and effectively; and 3) minimizing the time

Manuscript received 1 March 2024; revised 20 March 2024; accepted 22 March 2024. Date of publication 4 April 2024; date of current version 15 May 2024. This work was supported in part by the AI-Powered Manipulation System for Advanced Robotic Service, Manufacturing and Prosthetics (IntelliMan) Project: EU H2022 under Grant 101070136. The associate editor coordinating the review of this article and approving it for publication was Dr. Pedro Oliveira Conceição Junior. *(Corresponding author: Haydar Al Haj Ali.)*

Haydar Al Haj Ali, Yahya Abbass, Christian Gianoglio, and Maurizio Valle are with the Department of Electrical, Electronic, Telecommunications Engineering, and Naval Architecture (DITEN), University of Genoa, 16145 Genoa, Italy (e-mail: haydar.alhajali@edu.unige.it; yahya.abbass@unige.it; christian.gianoglio@unige.it; maurizio.valle@unige.it).

Ali Ibrahim is with the Department of Electrical and Electronics Engineering, Lebanese International University, Beirut 1105, Lebanon (e-mail: ali.ibrahim@liu.edu.lb).

Changjae Oh is with the Centre for Intelligent Sensing, Queen Mary University of London, E1 4NS London, U.K. (e-mail: c.oh@qmul.ac.uk).

This article has supplementary downloadable material available at https://doi.org/10.1109/JSEN.2024.3382369, provided by the authors.

Digital Object Identifier 10.1109/JSEN.2024.3382369

TABLE I
RELEVANT WORKS ON TACTILE TEXTURE CLASSIFICATION

Reference	Sensor	Encoding Model	Feature Extraction	Type of Features	Mechanoreceptors	Classifier
[13]	Piezoresistive	Izhikevich	Yes	Average firing rate (FR), Coefficient of variation (CO) of Inter-spike Interval (ISI)	SA-I	K-Nearest Neighbor
[14]	Piezoresistive	Izhikevich	Yes	Average FR, CO of ISI, Fano factor of spikes, Co-occurrence matrices	SA-I	k-Nearest Neighbor
[15]	Piezoresistive	Izhikevich	Yes	Average ISI, Average FR	SA-I	Support Vector Machine
[16]	Piezoresistive	Izhikevich	Yes	Time-delayed input signals	SA-I & RA-I	Extreme Learning Machine
[17]	PVDF	Izhikevich	Yes	Spike train distances	SA-I	k-Nearest Neighbor
[18]	PVDF	Poisson	Yes	Gray scale images	-	Spiking Neural Network
This work	**PVDF**	**Leaky-Integrate-Fire**	**No**	**-**	**SA-I & RA-I**	**Recurrent Spiking Neural Network**

latency of the hosting device [10] and match the biological range.

Various methods based on machine learning (ML) and deep learning (DL) approaches have been studied to analyze tactile data coming from tactile sensing systems, addressing both classification [19] and regression tasks [20]. These algorithms are hosted by dedicated edge accelerators near the sensors for fast and efficient inferences. The aforementioned approach has led to the development of a complete tactile system that is utilized in various tactile recognition tasks such as touch modality [21] and texture classification [22], object recognition [8], and Braille letter reading [23], [24].

Despite all these technological advances that optimized the performance of the artificial tactile sensing system, it remains distant from emulating the sensory capabilities of the human touch system [25]. The main reason behind this disparity is that biological systems can process even more complex information rapidly, efficiently, and with significant differences in energy consumption compared to the state-of-the-art systems [26]. Moreover, the artificial systems rely on conventional computers [27] (i.e., Von-Neumman-based) that, by their nature, cannot support rapid computations [28].

To address the aforementioned limitations, we employ a neuromorphic computing-based system inspired by the computational primitives found in the human somatosensory system, to bridge the efficiency gap between artificial systems based on conventional computing and their biological counterparts. Neuromorphic computing, unlike conventional systems, features brain-inspired computational primitives that are applied at the software and hardware levels, with the aim of emulating biological nervous systems [29], [30], [31]. This approach involves the conversion of analog signals into digital asynchronous spikes or events, carrying temporal and spatial information, therefore, modeling the mechanoreceptors of the skin. The emitted spikes can be exploited for classification tasks using spiking neural networks (SNNs), that simulate the neuronal spiking mechanism and plasticity observed in the somatosensory system [32], [33]. Neuromorphic circuits utilize mixed analog/digital hardware signals. This enables the implementation of these SNNs and fully exploits their intrinsic features. These features include event-driven processing, asynchronous communication between neurons, and learning based on local information [25], [34]. Therefore, the neuromorphic approach through its biologically inspired primitives is projected to optimize the artificial tactile sensing system through performing robust information processing with minimal use of hardware resources.

In this work, we focus on the classification of textural features of artificial gratings. The inherent time-dependent nature of the texture's signals [35] imposes difficult challenges during classification, such as capturing the significant temporal dependencies of the texture without relying on complex methods. This is further compounded by the requirement for rapid response in texture perception applications, such as tactile feedback systems, making it one of the most formidable challenges for artificial tactile systems [36].

B. Related Works

The human somatosensory system has been the inspiration of considerable works in the literature that addressed texture classification problems based on a neuromorphic approach. Table I provides an overview of some existing literature on tactile-based texture classification.

In general, these works model the firing behavior of the biological mechanoreceptors to transform tactile signals into spikes, followed by a feature extraction phase and then classification based on different classifiers. The proposed solutions demand offline processing of raw signals, such as requiring a whole window of signal (time window) to compute handcrafted features, before fetching the decision or action, which correspondingly requires high-computational resources such as memory footprint, power consumption, and high inference time. Despite the wide range of proposed features, varying from simple and basic features as in [13] and [15] to more complex features as in [14] and [17], the drawback persists,

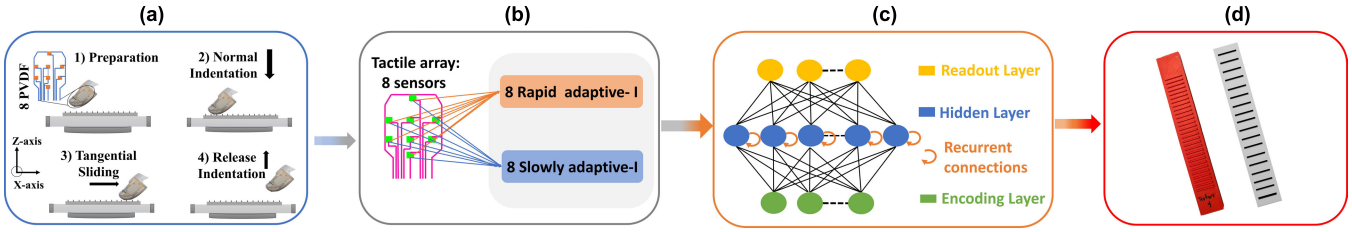

Fig. 1. Overview of the proposed neuromorphic tactile sensing system. (a) Data collection: indentation touches were applied at different velocities and forces. (b) Encoding of gratings' raw signals into spikes by modeling the slow and rapid adaptive mechanoreceptors. (c) Proposed RSNN for textural features classification. (d) Gratings' classification.

by requiring a time window of signal for processing. Furthermore, most of these works employed the Izhikevich model for encoding and spike conversion. Despite its efficiency and precision in modeling the cortical neurons' behavior, it primarily focuses on analyzing spike features (i.e., fine temporal structure). However, implementing it at the neural network level presents a drawback due to its computational cost [37]. Additionally, neglecting the temporal characteristics inherent in texture encoding and exclusively addressing it through rate-coding limits the generalizability of the proposed solution for complex tactile applications as in [16] and [18].

Most of the proposed solutions rely on piezoresistive sensing systems [13], [14], [15], [16], which are characterized by a low-frequency range response (<100 Hz) [38]. Conversely, few relevant works adopted a P(VDF-TrFE) poly(vinylidene fluoride trifluoroethylene)-based (PVDF) piezoelectric sensing system for the same application as in [17] and [18]. According to [11], PVDF sensors exhibit a wide frequency range ($\leq$ 1 Hz–1 kHz), due to their fast dynamic response (i.e., polymers crystallization), hence covering the range of the mechanoreceptors in the human skin [39]. However, the aforementioned solutions maintained offline-based complex methods for texture classification.

C. Contribution

In this work, we present a neuromorphic tactile sensing system for classifying the textural features of artificial gratings. The proposed system consists of a PVDF-based sensing system and neuromorphic classification framework that can be implemented in real time to process and classify tactile information as pictured in Fig. 1.

The main contributions of this article are summarized as follows.

1) We present a recurrent SNN (RSNN) for textural features classification. The RSNN is trained by the surrogate gradient descent (SGD) [40] to process raw signals and perform subsequent classification. Unlike the exciting methods in the literature (see Table I), the novelty of this work lies in classifying the artificial grating using the raw tactile signals obtained from the sensors, without the need to extract features.
2) We propose a strategy to control the computational cost and the classification accuracy of the RSNN, based on tuning the refractory period of the spiking neurons during the encoding. The strategy allows the selection of the network with a trade-off between the aforementioned metrics for real-time deployment.
3) The selected network is further optimized by reducing the number of simulation time steps in the inference using a rate-coding approach. This method allows to reduce the overall inference time and computational cost of the network.
4) We evaluated the proposed neuromorphic system under various experimental conditions, in particular, the sliding velocity and indentation force. To the best of our knowledge, this is the first study that undertakes such an assessment while employing a PVDF-based sensing system. The results demonstrate the robustness of the proposed solution to the aforementioned variation of sensing conditions.

The rest of this article is organized as follows. Section II describes the tactile sensing system and the experimental design. Section III presents the implemented neuromorphic methods. Section IV depicts the proposed optimization methods. Section V addresses the conducted experiments to evaluate the overall approach. Section VI reports the obtained results.

II. Materials

A. Sensing System and Experimental Setup

This study utilizes a PVDF-based sensing system originally developed for a prosthetic hand (see [10]). The system comprises a biomimetic finger equipped with a piezoelectric sensing array and embedded electronics. We adopted specifically the piezoelectric sensing array (eight sensing units) designed for the volar side of the distal phalanx of the index finger as shown in Fig. 2(b) (sensor distribution). The sensing units are screen-printed on a finger-shaped flexible PET substrate. Each sensing unit comprises a P(VDF-TrFE) poly(vinylidene fluoride trifluoroethylene) piezoelectric polymer layer, sandwiched between two PEDOT:PSS electrodes [see Fig. 2(b)]. The biomimetic finger was 3-D printed using thermoplastic polyurethane (TPU) material. The sensing array was shielded using conductive tapes and then attached to the finger using double-sided adhesive tape. Finally, a thin flexible cylindrical shape protective layer (Art. 5500 Dream, Framisitalia) has been added on the top of the sensing array forming a skin patch.

The embedded electronics presented in [41] were used to acquire, sample, and send tactile signals to a host PC. It comprises a 32-channel analog-to-digital converter DDC232 (Texas Instrument, US), and an ARM cortex-M0 low-power-based microcontroller. The embedded electronics samples at 2 KSamples/s/channel to cover the full frequency bandwidth (1 Hz–1 kHz) of the sensors.

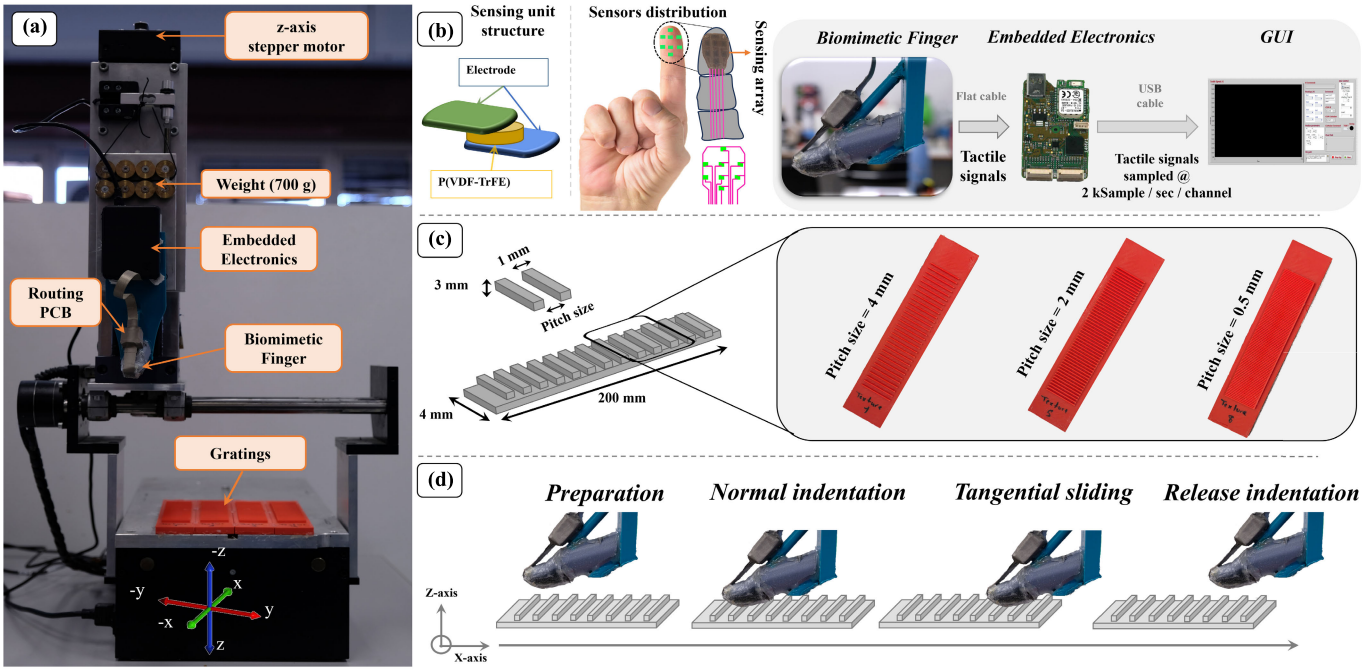

Fig. 2. Experimental setup for texture classification. (a) Three-axis Cartesian robot employed in controlled-environment data collection. (b) Sensor structure, distribution, and data processing. From left to right: Sensing unit structure and geometry. A biomimetic fingertip was sensorized with the sensing array and mounted to the z-axis of the robot along with the embedded electronics. (c) Artificial gratings design and geometry. Each grating was designed with a specific pitch size to control its coarseness level. (d) Illustration of the four phases of the data collection procedure.

A three-axis Cartesian robot was used to perform a series of sliding actions on the gratings along the x-axis [see Fig. 2(a)]. The biomimetic finger was connected to the embedded electronics through a flat cable and both were fixed on the z-axis as shown in Fig. 2(a). Each of the three axes of the Cartesian robot is driven by three stepper motors, controlling the xyz coordinates and the speed. To modulate the indentation load on the biomimetic sensor, a 700-g weight was mounted on the z-axis and hung to a spring. Data acquisition, visualization, collection, and control of the Cartesian robot were implemented using a graphical user interface (GUI) developed with NI LabVIEW on a host PC [see Fig. 2(b)].

B. Tactile Stimuli

A total of eight gratings were designed and 3-D printed using polylactic acid (PLA) [see Fig. 2(c)]. The plates host a series of 1-mm-thick and 3-mm height ridges separated by a pitch size (P) that varies between 4 and 0.5 mm with a decrement of 0.5 mm. Thus, varying gradually the coarseness level of the tactile stimuli from rough ($P = 4$ mm) to smooth ($P = 0.5$ mm). Section 1.1 and Fig. S1 in the Supplementary Material describe and illustrate the characteristics of the artificial gratings.

C. Experimental Protocol

The experiment consists of four main phases [see Fig. 2(d)].

1) *Finger Preparation:* The finger is located ∼1 cm above the grating (preparation stage).
2) *Normal Indentation:* The finger is indented to the surface of the grating for a period of ∼0.5 s with an indentation force F [N].
3) *Tangential Sliding:* The finger slides tangentially for 200 mm across the grated surface along the x-axis with a sliding velocity v [mm/s].
4) *Release Indentation:* After maintaining its position (end of the grating surface) for 0.5 s, the finger is then returned to its preparation position. This procedure is repeated 100 times for each grating.

To investigate and analyze the relation between the performance of the proposed neuromorphic system and the experimental conditions (sliding velocities and indentation forces), multiple experiments were performed with a range of parameters commonly explored in the literature [42]. These experiments encompassed two sliding velocities $v1 = 8.6$ mm/s (minimum achievable velocity along the x-axis) and $v2 = 13.7$ mm/s (maximum velocity). Additionally, three indentation forces were considered $F_{\text{low}} = 3$ N, $F_{\text{medium}} = 6$ N, and $F_{\text{high}} = 12$ N. In total, 600 trials are recorded in this study, consisting of six distinct experimental combinations, with each combination conducted 100 times per grating.

III. Methodology

This section presents the methods employed for textural features classification. First, we addressed the modeling procedure of the biological mechanoreceptors employed to encode the grating's raw signal into spikes. Following this, we presented the architecture of the RSNN employed for the classification along with the training algorithm and procedure.

A. Encoding

We modeled two mechanoreceptors innervating the Glabrous skin, specifically focusing on the Meissner corpuscle

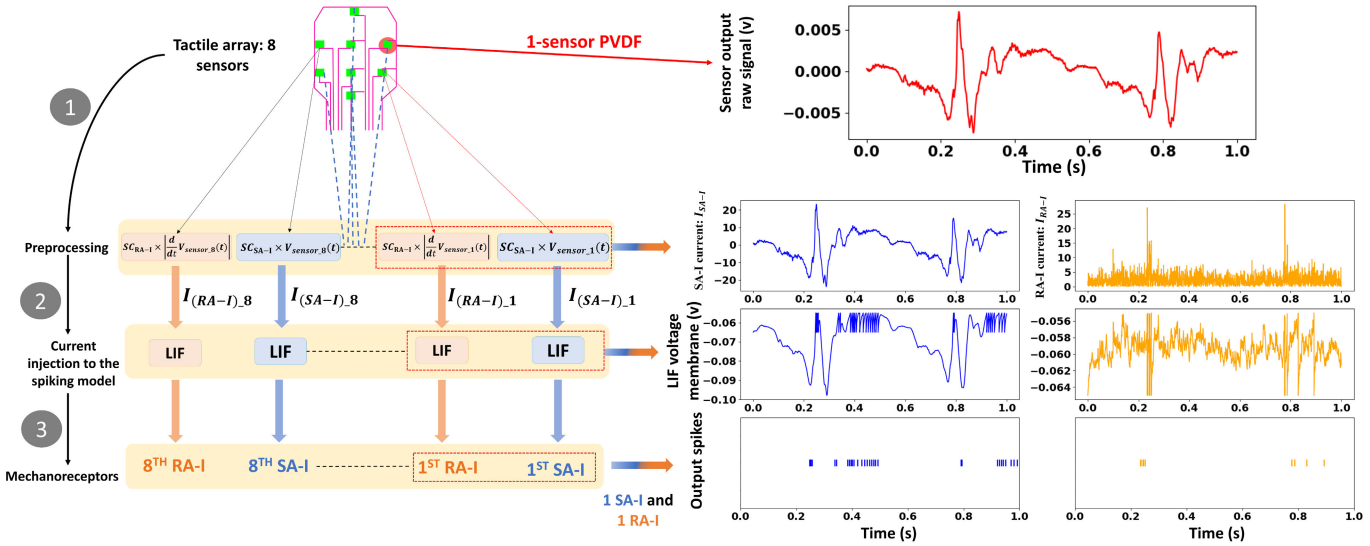

Fig. 3. Demonstration of the mechanoreceptors' (eight SA-I and eight RA-I) modeling procedure based on the eight sensors output raw signals. The currents of mechanoreceptors are computed through the constitutive equations in (2) and (3). These currents are then injected into the LIF neuron for encoding. The output raw signal of a one PVDF sensor for Grating 1, collected with $F = 12$ N and $v1 = 8.6$ mm/s) is involved in this illustration.

(rapid adaptive: RA-I) and the Merkel discs (slowly adaptive: SA-I) afferents. The motivation for this choice is to consider mechanoreceptors associated with texture perception with a minimal computational cost. The Ruffini ending (SA-II) is excluded as it is not implicated in texture perception [35], [43], [44]. RA-II was omitted due to its higher computational cost in modeling when compared to SA-I and RA-I receptors (refer to Section 1.2 in the Supplementary Material for details).

The output raw signals of the eight PVDF sensors are filtered by an exponential moving average (EMA) implemented as microcode in the embedded electronics to reduce signal noise online. A cut-off frequency of 30 Hz has been set based on the conducted frequency analysis of all textures across all the experimental conditions. The analysis revealed a spectral range of principal information between 1.8 and $\approx$ 10 Hz. Frequency analysis is reported in Section 1.3 in the Supplementary Material. Consequently, the filtered raw signals are fed to the artificial spiking neuron to be encoded and converted to digital spikes. The primary objective is not to mimic the human mechanoreceptors with utmost fidelity but rather to establish a straightforward framework for potential future hardware implementation. Therefore, this study focuses on modeling the mechanoreceptors with a balance between computational cost and the degree of precision in modeling. In this regard, we adopt the leaky-integrate-and-fire (LIF) neuron due to its lower computational cost compared to the Izhikevich neuron, which is widely used in relevant works [37]. The LIF neuron model is described as a dynamical time-continuous system [45]

$$\tau_m \frac{dU(t)}{dt} = -(U(t) - U_{\text{rest}}) + R_m * I_{\text{input}}(t) \quad (1)$$

where $U(t)$ is the voltage membrane potential that defines the state of the neuron, U_{reset} is the resting value, τ_m represents the membrane time constant, R_m is the input resistance (equal to 1 Ω for convenience), and $I_{\text{input}}(t)$ is the neuron's input current. When an input current $I_{\text{input}}(t)$ is applied, the membrane potential $U(t)$ undergoes a depolarization phase (accumulation of input current). Once $U(t)$ reaches a defined threshold V_{th}, the neuron emits a spike and the membrane potential is reset to U_{reset} for a defined time called refractory period t_{ref}. The parameter values of the LIF neuron are selected to approximate regular spiking behavior in neurons [46], [47], [48] to encode the dynamic and static stimulus [1]. Table II lists the parameter values.

TABLE II
PARAMETERS OF THE LIF MODEL

Parameter	U_{reset}	V_{th}	τ_m	t_{ref}
Value	-65 mV	-55mV	10 ms	[1-10] ms

Fig. 3 demonstrates the procedure of modeling the SA-I and RA-I mechanoreceptors. The raw signal of each PVDF sensor is employed to model a combination of two mechanoreceptors: one RA-I and one SA-I. Therefore, a total of eight RA-I and eight SA-I neurons, corresponding to the eight PVDF sensing units, are modeled and randomly distributed across the finger index (see Fig. 3). The modeling procedure is outlined sequentially as follows.

1) The output raw signal of each PVDF sensor undergoes a conversion into two distinct currents: $I_{\text{SA-I}}$ and $I_{\text{RA-I}}$ (step 1 in Fig. 3), using the following equations [16], [49]:

$$I_{\text{SA-I}} = \text{SC}_{\text{SA-I}} * V_{\text{sensor}}(t) \quad (2)$$

$$I_{\text{RA-I}} = \text{SC}_{\text{RA-I}} * \left| \frac{d}{dt} V_{\text{sensor}}(t) \right| \quad (3)$$

where $\text{SC}_{\text{SA-I}}$ and $\text{SC}_{\text{RA-I}}$ represent the scaling coefficients of currents $I_{\text{SA-I}}$ and $I_{\text{RA-I}}$, respectively, and

$V_{\text{sensor}}(t)$ represents the output raw signal of the sensors at time t.

2) The two currents $I_{\text{SA-I}}$ and $I_{\text{RA-I}}$ are applied to the LIF neuron as an input $I_{\text{input}}(t)$ in (1) (step 2 in Fig. 3).
3) The LIF voltage membrane undergoes a depolarization through the accumulation of the two currents until it reaches V_{th}, triggering the emission of a spike (step 3 in Fig. 3).

Following the same procedure of [13], [14], and [16], the optimum scaling coefficients (SC) values $\text{SC}_{\text{SA-I}}$ and $\text{SC}_{\text{RA-I}}$ are selected based on the interspike interval (ISI) distribution of the neuron model in response to the gratings stimuli with different SC values. The considered SC values ranges are $\text{SC}_{\text{SA-I}} = [1800, 3200, 6400]/\text{M}\Omega$ and $\text{SC}_{\text{RA-I}} = [18\,000, 32\,000, 64\,000]/\text{M}\Omega$. Generally, increasing the SC value in both neurons typically results in an increased firing rate (FR) and a consequent decrease in the ISI. The ISI decrease yields an overlapping distribution of the ISI associated with different gratings, leading to a close spiking response. Conversely, decreasing the SC value leads to a low FR and a substantial loss of information (due to the high sparsity). This, in turn, leads to an increase in both the values and distribution of the ISI in addition to an increase in response latency. Therefore, the selected SC values are $\text{SC}_{\text{SA-I}} = 3200/\text{M}\Omega$ and $\text{SC}_{\text{RA-I}} = 32000/\text{M}\Omega$, carrying a compromise between the issues above (see Fig. S3 in Section 1.4 in the Supplementary Material).

B. Recurrent Spiking Neural Networks

1) Architecture and Design: We designed a two-layer RSNN inspired from [50] to perform classification as shown in Fig. 1(c).

The network consists of an encoding layer (green) with 16 LIF neurons (eight SA-I and eight RA-I receptors, see Section III-A), a hidden layer (blue) with recurrent connections (orange) among a pool of neurons $\text{Ni} = \{20, 30, 40, 50\}$ for model selection (to choose the best Ni based on performance/computational cost trade-off), and a readout layer including eight LIF neurons to classify the eight gratings. The neurons of the readout layer (yellow) decode the spiking activity to their corresponding grating based on maximal spike count (rate-coding), in which the winning neuron is the one with the highest number of emitted spikes.

The neurons in the hidden and output layers are based on the current-based (CUBA) LIF neuron written in discrete time as

$$U_i(t+1) = \beta\left(U_i(t) + I_i(t)\right) \cdot \left(1 - U_{\text{reset}}\right) \tag{4}$$

where U_i is the voltage membrane potential of the ith neuron, U_{reset} is the resting voltage, β is the voltage membrane decay set as a hyperparameter [51], and I_i is the synaptic current that carries the emitted spikes to the downstream neurons. t is used to represent the time step t_{steps}. The choice behind adopting the CUBA LIF neuron is supported by Bouanane et al. [52] which demonstrated the efficient exploitation of the temporal dynamics by this neuron through its exponentially decaying synaptic current $I_i(t)$. The postsynaptic current $I_i^{(l)}$ of ith neuron in layer l is modeled as

$$I_i^{(l)}(t+1) = \alpha I_i^{(l)}(t) + \sum_j W_{ij} S_i^{(l-1)}(t) + \sum_j V_{ij} S_i^{(l)}(t) \tag{5}$$

where α represents the current decay constant and considered as a hyperparameter, W_{ij} and V_{ij} are, respectively, the forward and recurrent learnable weights within each layer, and $S_i^{(l)}(t)$ is the spike train of the ith neuron in layer l denoted as a binary step function as follows:

$$S_i^{(l)}(t) = \Theta\left(U_i(t) - \phi\right) \tag{6}$$

where the firing threshold $\phi = 1$ [40] (parameters discussion in Section 1.5 in the Supplementary Material).

Initially, the raw signals are fed to the encoding layer as a 2-D tensor with size $t_{\text{steps}} \times N_s$, where t_{steps} (time steps) $= Fc * T$, $Fc = 2\text{KSample/s}$, T is the input raw signal duration in seconds, and $N_s = 8$ corresponds to the number of sensors of the patch. Consequently, the generated spikes from the encoding layer (see Fig. 3) will be forwarded to the RSNN [see Fig. 1(c)] as a 2-D tensor with size $t_{\text{steps}} \times 2 * N_s$ to be decoded and classified, where the $2 * N_s$ is the number of LIF neurons modeling the SA-I and RA-I mechanoreceptors.

2) Surrogate Gradient Descent: The SGD presented by Neftci et al. [40] is employed to train the RSNN to classify the textural features of the gratings directly from the emitted spikes without using hand-crafted features. This supervised learning approach was introduced to solve the non-differentiability issue of the spike activation and back-propagate the error throughout the network using back-propagation through time (BPTT). The method works by maintaining the non-differentiable step function during the inference of the RSNN (forward pass with trained parameters) and replaces it with a differentiable function to compute its gradient during the backward pass and update the learnable weights of the network (W_{ij} and V_{ij}) using the chain rule [53]. We used the gradient (partial derivative) of the fast sigmoid function $\sigma(x)$ (7) during the backward pass in this work

$$\sigma\left(U_i^{(l)}\right) = \frac{U_i^{(l)}}{1 + \lambda |U_i^{(l)}|} \tag{7}$$

where λ is the scale parameter of $\sigma(x)$, and considered a hyperparameter to be tuned based on the spiking activity of the stimuli. A custom function has been designed in Pytorch [40], [50] for the SGD implementation (SGD mathematical discussion in Section 1.6 in the Supplementary Material).

3) Training Setup and Strategy: For network training, a 70%/15%/15% is chosen for the training/validation/testing split, while maintaining balanced sets for the eight classes. The investigated datasets are elaborated in Section V. The networks are trained with a learning rate $\text{lr} = 0.001$ and batch size $= 128$ for 100 epochs. The neural network intelligence (NNI) toolkit [54] is used for the hyperparameter optimization (HPO), and model selection, over 800 trials (check Section 1.7 in the Supplementary Material for HPOs list and description). The best-performing hyperparameters (in terms of classification accuracy) are selected based on the validation accuracy (intermediate result in NNI), and then

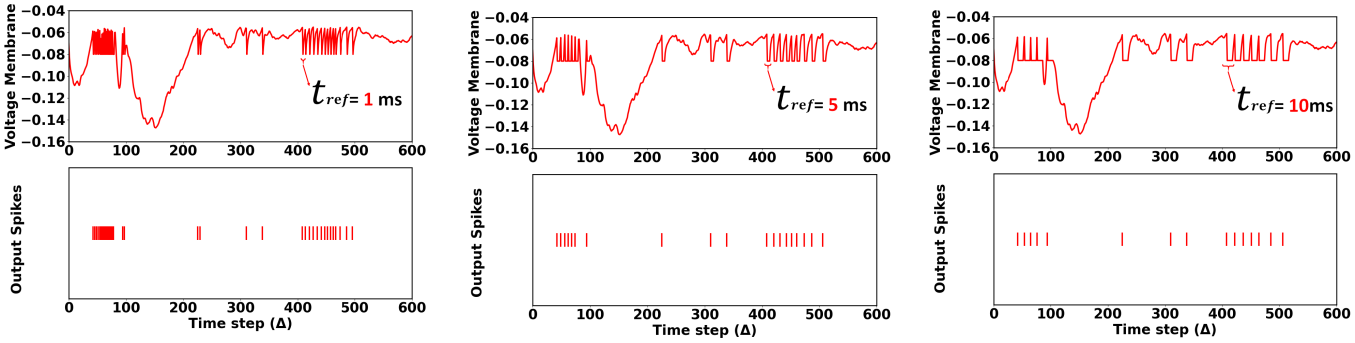

Fig. 4. Impact of changing t_{ref} on the behavior of the voltage membrane potential and spiking activity of the LIF neuron using the same raw input. (a) $t_{\text{ref}} = 1$ ms (spike count = 38), (b) $t_{\text{ref}} = 5$ ms (spike count = 19), and (c) $t_{\text{ref}} = 10$ ms (spike count = 15). Top: Voltage membrane dynamics of the LIF neuron. Bottom: Raster plot or spiking activity of the LIF neuron.

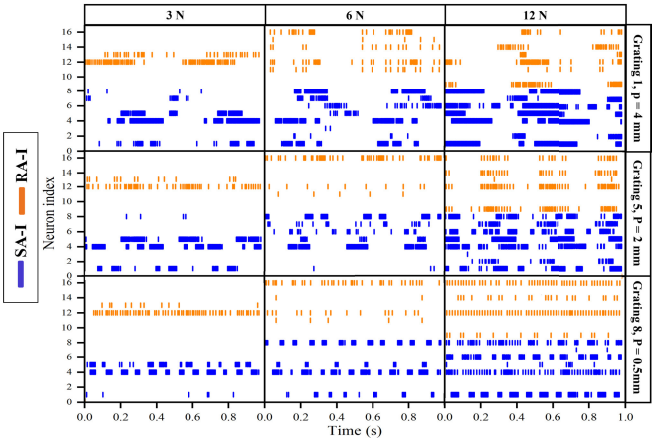

Fig. 5. Raster plot showing the spiking activity of the eight SA-I (blue) and eight RA-I (orange) mechanoreceptors for Gratings 1 ($P = 4$ mm), 5 ($P = 2$ mm), and 8 ($P = 0.5$ mm). The plots illustrate the impact of the three forces at sliding velocity $v1$.

evaluated for generalizability using the testing set (final result in NNI). The early stop criterion is involved during training to avoid over-fitting, by monitoring the validation loss with patience = 7.

4) Computational Cost Estimation: The computational cost of the RSNN is estimated as the total number of synaptic operations (SOPs) of the network. The SOPs are computed using the methods presented in [55] by calculating the number of SOPs $Q^{(l)}$ for each layer

$$Q^{(l)} = f^{(l+1)} \sum_i a_i^{(l)} \tag{8}$$

where $a_i^{(l)}$ denotes the spiking activity of ith neuron in layer l, $f^{(l+1)}$ represents the number of neurons in layer $l+1$ that receive the spikes emitted by a single neuron in layer (l). Following this, the total SOPs of the network are obtained by summing $Q^{(l)}$ of all layers:

$$\text{SOPs} = \sum_l Q^{(l)}. \tag{9}$$

IV. Optimization

This section illustrates the optimization methods proposed to reduce the computational cost of the RSNNs while maintaining classification accuracy. Initially, we explored the concept of the refractory period t_{ref} in spiking neurons, examining its influence on the spike count and information. Following, we exploited this concept to optimize the proposed RSNN with a list of t_{ref} combinations. Finally, we addressed another optimization method focused on decreasing the RSNN simulation time steps through a rate-coding approach.

TABLE III
Proposed Refractory Periods

Notation ($t_{\text{ref}_{\text{RA-I}}}$ & $t_{\text{ref}_{\text{SA-I}}}$)	Mechanoreceptors	
	RA-I	SA-I
1&1	1 ms	1 ms
5&5	5 ms	5 ms
10&10	10 ms	10 ms
1&5	1 ms	5 ms
1&10	1 ms	10 ms
5&10	5 ms	10 ms

A. Refractory Period Fine-Tuning

The refractory period, or t_{ref}, is the duration that the spiking neuron in the somatosensory cortex undergoes a silent mode after spike emission, in which the membrane potential $U(t)$ remains at its resting value U_{reset} for a defined period [56], [57]. We employed t_{ref} to control the number of emitted spikes during encoding. The goal is to investigate the optimal t_{ref} that enables the mechanoreceptors to transmit sufficient information to downstream neurons in the RSNN (hidden and readout layer neurons) with a minimal computational cost (in terms of the number of spikes emitted). Fig. 4 shows the impact of t_{ref} on the number of emitted spikes while applying random input to the LIF neuron. Increasing t_{ref} [see Fig. 4(b) and (c)] results in a longer silent period after spike emission. Thereby, reducing the spiking activity and hence the number of SOPs (computational cost). However, this comes at the cost of a higher information loss, due to the ignored applied input during this period. In contrast, decreasing t_{ref} results in a shorter duration where the neuron is inactive or silent, leading to increased spike emission, higher computational cost, and reduced information loss [see Fig. 4(a)].

A list of six combinations of t_{ref} for SA-I and RA-I mechanoreceptors during the encoding phase is proposed in

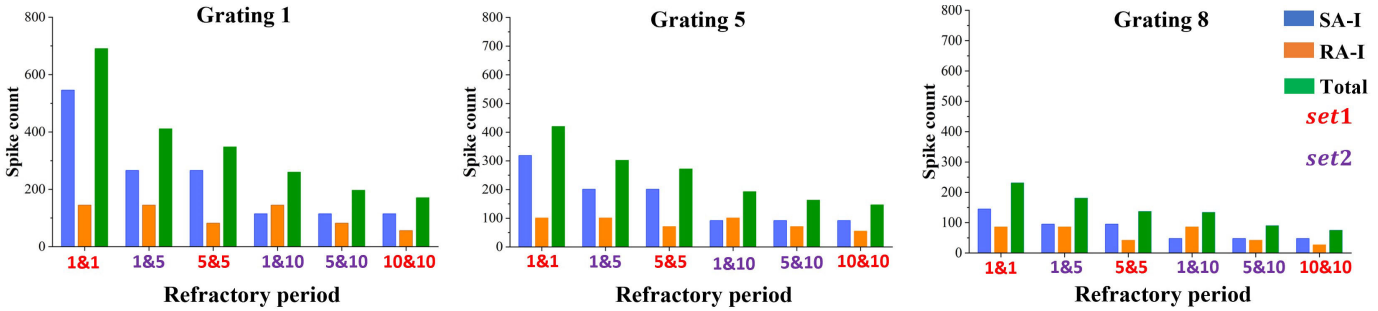

Fig. 6. Impact of the proposed t_{ref} combinations (set1 and set2) on the spike count for SA-I (blue) and RA-I (orange) for an input of 1 s. The spike count for both receptors illustrated their contribution to the total number of spikes (green). The three plots show the impact on gratings: grating 1 (left), grating 5 (middle), and grating 8 (right), at $F = 12$ N and *v1*. For the sake of visualization, the t_{ref} combinations where sorted in descending order.

Table III, and notated as ($t_{\text{ref}_{\text{RA-I}}}$ and $t_{\text{ref}_{\text{SA-I}}}$). The combinations cover a range from 1 to 10 ms, encompassing the typical range observed in cortical neurons [56], [57]. The combinations are classified into set1 and set2. In particular, set1 includes combinations with the same t_{ref} for both SA-I and RA-I mechanoreceptors during the encoding [e.g., 1&1 ($t_{\text{ref}} = 1$ ms for SA-I and RA-I), 5&5 ($t_{\text{ref}} = 5$ ms), and 10&10 ($t_{\text{ref}} = 10$ ms)]. While set2 incorporates combinations with different t_{ref} for SA-I and RA-I [e.g., 1&10 (1 ms for RA-I and 10 ms for SA-I), 1&5 (1 ms for RA-I and 5 ms for SA-I), and 5&10 (5 ms for RA-I and 10 ms for SA-I)]. The motivation behind the proposed combinations in the set2 relies on the firing dynamics of both mechanoreceptors. Fig. 5 shows the effect of the indentation force on the spiking activity of both mechanoreceptors across grating 1 (rough), grating 5 (intermediate), and grating 8 (smooth). In general, SA-I neurons consistently exhibit a higher spiking activity (emitted spikes) compared to RA-I neurons. Hence, the set2 is proposed to significantly reduce the spiking activity of the former neurons while partially mitigating the activity of the latter. This is intended to achieve an approximate balance between both mechanoreceptors and to study the contribution of each, in terms of the conveyed encoded information. The effect of co-varying the t_{ref} and the SC values of currents $I_{\text{SA-I}}$ and $I_{\text{RA-I}}$ for both mechanoreceptors is reported in Section 1.8 and Fig. S4 in the Supplementary Material.

Fig. 6 shows the effect of each proposed combination during the encoding phase in terms of spike count for SA-I and RA-I. The tactile signals of three gratings with a salient difference in coarseness level have been investigated for simplicity. As expected, the 1&1 combination generated the highest number of spikes in comparison to the others, since both receptors (SA-I and RA-I) are inactive for the smallest period after spike emission (i.e., 1 ms), thus increasing the number of computations. Conversely, the 10&10 combination exhibits the lowest spike count. This can be attributed to its longer no-activity period, leading to occasional spiking activity. Straightforwardly, the 5&5 combination falls between the two previous values. The repetitive behavior of the three combinations can also be observed in grating 1 (roughest), grating 5 (intermediate), and grating 8 (smoothest), with a variation in the overall spike count.

TABLE IV
DATASETS UTILIZED IN THE EXPERIMENTS

Dataset	Force (N)			Velocity (mm/s)	
	3	6	12	v1 = 8.6	v2 = 13.7
$D_{v1,L}$	✓			✓	
$D_{v1,M}$		✓		✓	
$D_{v1,H}$			✓	✓	
$D_{v1,mix}$	✓	✓	✓	✓	
$D_{v2,L}$	✓				✓
$D_{v2,M}$		✓			✓
$D_{v2,H}$			✓		✓
$D_{v2,mix}$	✓	✓	✓		✓
D_{mixed}	✓	✓	✓	✓	✓

To examine the t_{ref} combinations of set2, it is necessary to visualize and compare the individual contributions of the SA-I and RA-I receptors. The two combinations 1&10 and 5&10 exhibited a total spike count that falls between the two combinations 5&5 and 10&10. Additionally, the 1&5 combination achieves the second-highest spike count, following the 1&1 one. It can be observed in the two combinations 1&5 and 5&10 that SA-I receptors overcome RA-I receptors in terms of the number of emitted spikes despite the smaller t_{ref} assigned to the RA-I. The only combination that witnessed opposite action is 1&10, as RA-I receptors emitted more spikes due to the 9-ms difference between the assigned periods. Hence, the SA-I receptors play a predominant role during the encoding process (in terms of spike count).

B. Reducing Inference t_{steps} of RSNN

The RSNN's readout layer decodes the weighted spiking activity from the early layers during the forward pass using a spike count-based procedure for gratings classification, so-called RSNN inference. This method relies on rate coding, where the neuron emitting the highest number of spikes within a window of RSNN's time steps t_{steps} [t_{steps} is defined in Section III-B1, see (4)] is selected as the decoder for the input stimuli (provides the classification label). In this work, we introduce a new method to identify the neuron with the highest spike count without requiring the entire t_{steps}. The main motivation behind this is to investigate the possibility of

Algorithm 1 Reducing Inference t_{ref}

Input:
- Decoded Spiking Tensor T_D = [Time_steps × 8]
- $index\_true$, $Patience$

1.**Methodology**

do
  $M = T_D[1, :]$
  $i_{max}\_prev = argmax(M)$
  $count = 0$
  set $Patience$
  for $(i = 2; i \leq Time\_steps; i++)$ **do**
    $M = \sum_{j=1}^{i} T_D[j, :]$
    $i_{max} = argmax(M)$
    if $i_{max} == i_{max}\_prev$ **then**
      $count++$
      if $count == Patience$ **then**
        $Time\_new = i$
        $index\_op = i_{max}$
        break
      end if
    else
      $counter = 0$
      $i_{max}\_prev = i_{max}$
    end if
  end for
while $(index\_op \neq index\_true)$

2. Return $Time\_new$

reducing the number of t_{steps}, thereby decreasing the overall complexity and the inference time of the network for real-time deployment.

Algorithm 1 illustrates the proposed method. During each time step t_{step}, the neurons in the readout layer update their states by either a spike emission {1} or no spike emission {0}. A decoded spiking tensor T_D with size $t_{\text{steps}} \times N_{\text{out}}$ (N_{out} represents the neurons in the readout layer) stores the aforementioned updates (spike or no spike) according to the time step sequence. The method starts by selecting the neuron index with the highest spike count (i_{max}_prev in step 1.3) at the first time step (for initialization). Afterward, the algorithm computes the cumulative sum of the spike data stored in the T_D tensor for the N_{out} neurons ($N_{\text{out}} = 8$), starting from the preceding time steps (step 1.7). This process results in an array M that holds the spike count for each neuron over time. Next, the algorithm identifies a new variable i_{max} associated with the highest spike count selected from M (step 1.8). The algorithm then checks if i_{max} is equal to the initialized i_{max}_prev for a predefined period specified by the patience value (Patience). When this condition is met, the method returns two values: 1) index_op that is the neuron index with the maximum spike count i_{max} and 2) Time_new equal to the time step where the condition is met. If this condition is not fulfilled, the counter will be reset and start counting when the condition is met again. However, if the obtained index_op does not match the true decoding index index_true fetched during the training procedure, the entire process will be repeated by adjusting the Patience until the condition at step 1.21 is achieved. The neural network will be simulated along this optimized Time_new during inference.

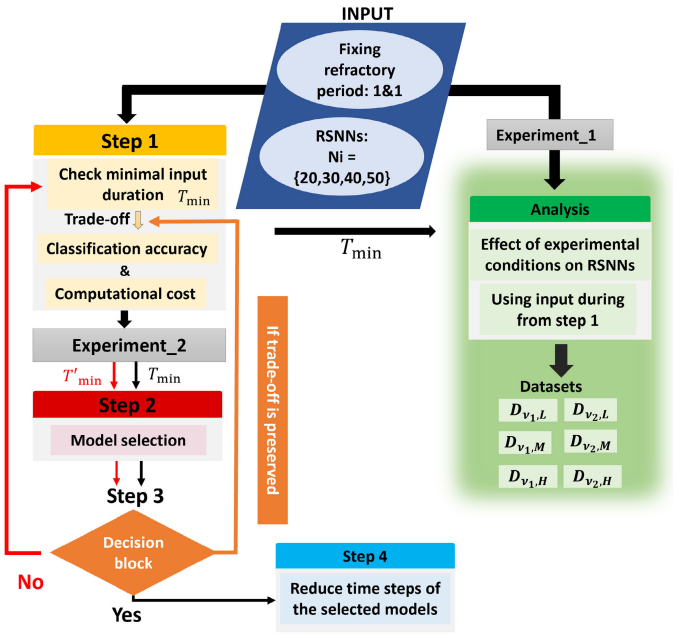

Fig. 7. Flow of experimental results. Description of *Experiment*_1 (right) and *Experiment*_2 (left).

V. Experiments

Two experiments are conducted in this article: 1) $Experiment\_1$: analyzing the impact of varying the experimental conditions (sliding velocities and indentation forces) on the performance of the proposed networks (before applying the suggested optimization methods) addressing each condition individually and 2) $Experiment\_2$: implementing the proposed optimization methods on the designed RSNNs to elicit the network with the best trade-off between the classification accuracy and computational cost for future real-time hardware deployment. The first part of the study utilizes six datasets (see Table IV). Three of these datasets, $D_{v1,L}$, $D_{v1,M}$, and $D_{v1,H}$, incorporated tactile information collected with $v1 = 8.6$ mm/s and forces = 3, 6, and 12 N, respectively. The other three datasets, $D_{v2,L}$, $D_{v2,M}$, and $D_{v2,H}$, used $v2 = 13.7$ mm/s and the same forces. The second part of the study merged the six datasets into three new datasets (see Table IV) as follows: $D_{v1,\text{mix}}$ combines all forces collected with $v1$, $D_{v2,\text{mix}}$ includes all forces collected with $v2$, and D_{mixed} merges all forces and velocities. The motivation behind this selection is to challenge the entire neuromorphic approach in complex experimental conditions, as preparation for future real scenarios where the conditions are unknown and unpredictable.

VI. Results and Discussion

The flow of the results is illustrated in Fig. 7. We started from a fixed input including a 1&1 t_{ref} combination along with all the designed RSNNs. We first explored the minimal input duration T_{min} that can be used to train the RSNNs, employing the aforementioned fixed input. Following this, the

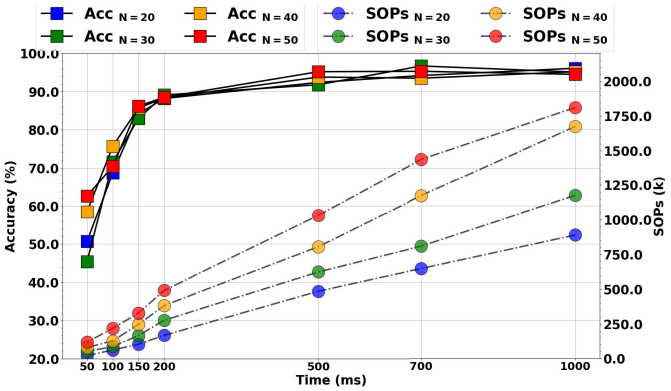

Fig. 8. T_{min} selection before optimization and network selection (step 1 in Fig. 7). The selection is based on a trade-off between classification accuracy and computational cost using the dataset D_{mixed}. The aforementioned dataset is selected for this experiment since the proposed neuromorphic system is designed to deal with all the experimental conditions (indentation forces and sliding velocities). N represents the hidden layer size of the RSNNs. Acc denotes the accuracy and SOPs stand for the number of SOPs in the legend.

selected T_{min} is used in $Experiment\_1$ and $Experiment\_2$ (see Section V).

A. Minimal Input Duration Selection T_{min}

According to [21] and [58], the input size impacts directly the computational cost of the neural network since larger input sequences require more computations to be performed. Therefore, it is crucial to explore the minimal input duration (i.e., the sliding duration) that carries sufficient information to the system to perform successful classification. To select T_{min}, a set of gradually increasing input raw signal sizes $T = \{.05, .10, .15, .20, .50, .70, 1.0\}$ s are evaluated in terms of classification accuracy and computational cost (number of SOPs). D_{mixed} (see Table IV) is used here while relying on the fixed input illustrated in Fig. 7 (1&1 t_{ref} combination along with all the designed RSNNs). Fig. 8 presents the selection procedure.

As shown in Fig. 8, all the RSNNs (Ni = 20, 30, 40, and 50) demonstrate consistent classification accuracy acc $\geq$ 92% with a time window $T \geq 200$ ms. This indicates that the essential spatiotemporal information of the gratings is adequately captured and repeated throughout the entire experiment. However, the computational cost of the network is affected by the size of the input, thereby a large input size yields a higher computational cost. This is validated when examining the total number of SOPs for each network that is increasing with the increase in the input size. A significant drop in performance is observed when evaluated with a shorter time window ($T \leq 100$ ms), resulting in accuracy ranging from 46% to 77%. This drop is related to the insufficient information within this T for the networks to effectively learn and classify the gratings. Based on this observation, the minimal time window T_{min} should fall between 100 and 200 ms. By taking into account the three evaluation metrics: classification accuracy, computational cost (SOPs), and latency, an input duration of 150 ms represents the best choice. This selection is motivated by the slight decrease in average accuracy $\approx$ 3% and $\approx$ 8% in the number of SOPs, and finally the gain of 50 ms in latency in comparison to what has been achieved using a 200-ms input duration. Therefore, $T_{\text{min}} = 150$ ms is selected as a convenient input size to the RSNNs and to be used accordingly in $Experiment\_1$ and $Experiment\_2$.

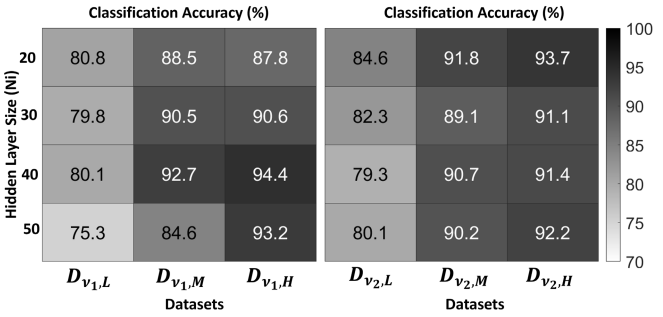

Fig. 9. Classification accuracy of the proposed models under all the experimental conditions. Left: Datasets collected with $v\mathbf{1} = 8$ mm/s. Right: Datasets collected with $v\mathbf{2} = 13.7$ mm/s. The refractory period t_{ref} involved here is 1 ms for both receptors.

B. Effect of Experimental Conditions

The investigation into the influence of the experimental conditions on the performance of the proposed RSNNs has been conducted using the selected $T_{\text{min}} = 150$ ms and with the fixed input (1&1 t_{ref} combination, since the goal is not to optimize the network at this point) as shown in Fig. 7 (right). Fig. 9 provides an overview of the best-achieved results by the RSNNs (with varying numbers of neurons N_i in the hidden layer) across all the experimental conditions (three indentation forces and two sliding velocities). The best configurations in terms of classification accuracy correspond to the datasets with high indentation forces (i.e., $F = 12$ N) in both sliding velocities: $D_{v1,H}$ and $D_{v2,H}$ (i.e., acc $\geq$ 90%, except RSNN with Ni = 20 in $D_{v1,H}$, i.e., acc = 87.8%), with a slight increase in accuracy in the latter. On the other side, the RSNNs exhibit a lower accuracy in classifying the gratings with datasets collected with low indentation forces (i.e., $F =$ 3 N): $D_{v1,L}$ (acc $\leq$ 81%) and $D_{v2,L}$ (acc $\leq$ 84%).

To discuss more, we computed the firing rate FR (Hz) $= n_{\text{sp}}/T_{\text{FR\_window}}$, where n_{sp} is the number of emitted spikes in a defined time window $T_{\text{FR\_window}}$ window (we used 150 ms). Additionally, we calculated the inter-spike interval: ISI (s) $= t_{s_{(t+1)}} - t_{s_{(t)}}$ where $t_{s_{(t+1)}}$ and $t_{s_{(t)}}$ represent the time of the following and preceding spikes respectively. Fig. 10 reports the computed encoding features (FR and ISI) for both mechanoreceptors across all gratings and experimental conditions. The overall normalized firing rate (Fig. 10(a)) reveals that an increase in the indentation force results in higher FR for both mechanoreceptors across all grating, and a decrease in ISI (Fig. 10(b)). Besides, increasing the sliding velocity yield a slight increase in the FR and accordingly the accuracy as shown in Fig. 11 (discussed in details in Section VI-C). This can be attributed principally to the amplitude of the output raw signal of each grating which increased remarkably when higher indentation forces were applied, and that induced a higher spiking activity for both receptors as shown in Fig. 12 and Fig. S5 in supplementary material section 1.9. For that

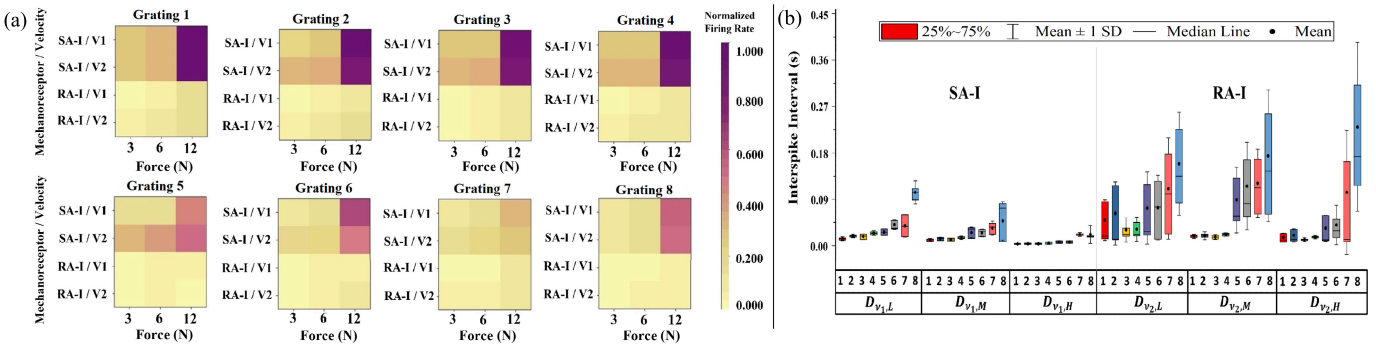

Fig. 10. SA-I and RA-I firing dynamics across all gratings and experimental conditions. (a) Impact of varying the experimental conditions on the FR of SA-I and RA-I neurons. Each matrix illustrates the normalized average FR obtained with a 150-ms time window, for each grating under all the performed sensing conditions (three indentation forces and two sliding velocities). (b) Computed average ISI for RA-I (right) and SA-I (left) using a 1-s data sample for each grating (gratings are denoted with their number (1:1:8), i.e., Grating 1:1, Grating 2:2, Grating 3:3, etc). The computations were carried out for the datasets $D_{V1,L}$, $D_{V1,M}$, and $D_{V1,H}$.

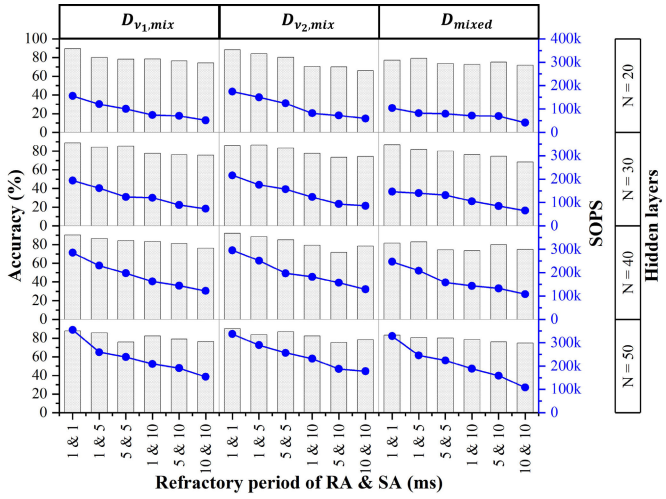

Fig. 11. Comparison of the evaluation metrics for the RSNNs in terms of classification accuracy (left column) and the number of SOPs (right column) when evaluated with the proposed t_{ref} combinations. All the RSNNs are trained and tested using the merged datasets mentioned in Table IV for generalization among all the experimental conditions. The networks are sorted by the evaluation metrics in descending order.

reason, higher classification accuracy is observed with the same conditions (using $D_{v1,H}$ and $D_{v2,H}$) due to the higher induced information. Conversely, a low FR is remarked for indentation force $F = 3$ N in both sliding velocities (due to the lower amplitude of the raw signal (Fig. 12 row 1)), thus leading to a drop in classification accuracy (accuracies obtained in $D_{v1,L}$ and $D_{v2,L}$), due to the poor representative information.

Generally, according to the computed encoding features and obtained results, it is noticed that the amplitude of the sensors' raw signal plays a vital role in reflecting the spatial shape of the grating and thereby its coarseness level, which aligns as well with the findings in [13]. Furthermore, increasing the sliding velocity did not demonstrate any significant effect on the induced FR of the mechanoreceptors across all gratings, and consequently the classification accuracy. Although increasing the sliding velocity from $v1 = 8.6$ mm/s to $v2 = 13.7$ mm/s (factor of $\approx$1.6) yields an increase in the principal frequency of each grating with the same factor ≈ 1.6 (refer to Table S1 in Section 1.3 in the Supplementary Material), this was not translated in terms of encoding. Particularly, $v2$ exhibited a slight increase in the FR compared to $v1$ as shown in Fig. 10(a). This observation can be linked to the slight increase in the amplitude of the raw signal corresponding to the increase in sliding velocity (see Fig. S6 in Section 1.10 in the Supplementary Material). In contrast, increasing the indentation force does not influence the principal frequency of the gratings. Instead, it affects the FR and the performance of the RSNNs. Hence, our system displays less dependence on speed and a greater dependence on high force in textural features classification.

C. Network Optimization and Selection

Following the guidance in Fig. 7, we implemented the proposed optimization methods in Section IV on the fixed input (1&1 t_{ref} combination with all RSNNs) after choosing T_{min}. We selected networks that demonstrated the best trade-off between computational cost and classification accuracy. Afterward, we examined whether the same trade-off achieved in step 1 was maintained by the selected networks in step 2 (Decision block). If the trade-off persisted, the selected networks proceeded to the final optimization stage involving a reduction in time steps during inference. If not, a new T_{min} is checked.

1) Refractory Period Fine-Tuning: Fig. 11 summarizes the obtained results after HPO. Each column in Fig. 11 represents the dataset (see Section V), with the t_{ref} combinations on the x-axis. The rows display the RSNNs, along with their corresponding hidden layer size (Ni).

The overall behavior of the networks follows the trend discussed in Section IV-A, and highlights the significant impact of tuning the refractory period t_{ref} at the network level. The combinations that display high spike emission (i.e., 1&1 and 1&5, see Fig. 6) enable all RSNNs to attain the highest classification accuracy across the three investigated datasets. These results can be attributed to the fact that smaller t_{ref} allows the modeled mechanoreceptors in the encoding layer to convey grating information more frequently and sufficiently to the hidden layer. This is a result of their short silent period

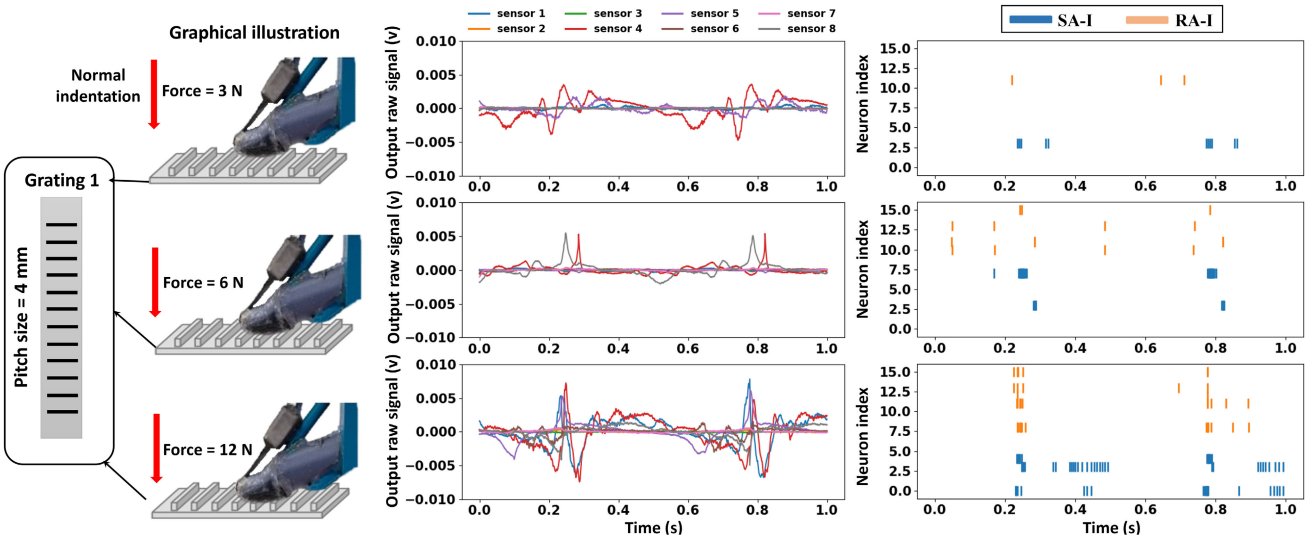

Fig. 12. Impact of increasing the indentation force (F) on the output raw signal and the encoding procedure (response of SA-I and RA-I mechanoreceptors). Grating 1 (pitch size = 4 mm) is considered in this illustration. Left: Graphical illustration of increasing the indentation force procedure during data collection. Middle: Output raw signals of the eight PVDF sensors. Right: Raster plot of the eight SA-I and eight RA-I modeled mechanoreceptors. Row 1: Force = 3 N. Row 2: Force = 6 N. Row 3: Force = 12 N. Each force is accompanied by $v\mathbf{1} = 8.6$ mm/s.

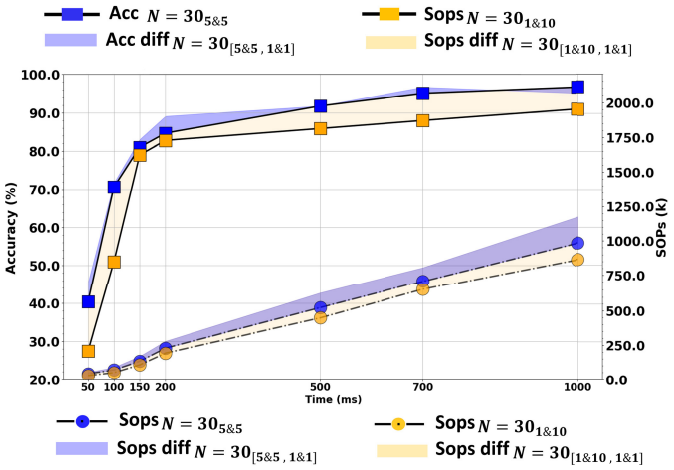

Fig. 13. Checking the persistence of the trade-off achieved in step 1 using the selected networks in step 2. He shaded area represents the difference between the initial and selected networks.

after spike emission, as depicted in Fig. 4(a). Nonetheless, this comes with the cost of a high number of SOPs. On the other side, the combinations with low spiking activity (i.e., 10&10, 5&10) yield the worst classification accuracy, due to the long silent period after spike emission leading to information loss [see Fig. 4(c)]. For example, the best classification accuracy in $D_{v_1,\text{mix}}$ (i.e., acc = 90.2%), $D_{v_2,\text{mix}}$ (i.e., acc = 92.1%), and $D_{v_{\text{mixed}}}$ (i.e., acc = 86.7%) corresponds to the combination 1&1 with Ni = 40, Ni = 40, and Ni = 30 neurons in the hidden layer, respectively. However, it is characterized by a high number of SOPs that affect future real-time deployment on a hardware device (i.e., increase inference time and power consumption during real-time classification). Alternatively, the worst performance in accuracy is coupled with combinations 10&10 and 5&10, resulting in a decrease of ≈15% and ≈10%, respectively.

Considering the two evaluation metrics (i.e., accuracy and computational cost), it is evident that the optimal combinations

TABLE V
OPTIMIZED TIME STEPS (TIME_NEW) AND PATIENCE VALUE FOR THE CHOSEN COMBINATIONS

Combination	Time_new (± std)	Patience
5&5	220 (±26)	120
1&10	238 (±32)	120

of t_{ref} presenting the best trade-off among the rest are those employing 5&5 and 1&10. For instance, the best-achieved accuracy by the 5&5 combination is 85.3% with Ni = 30 in $D_{v1,\text{mix}}$, 84.2% with Ni = 40 in $D_{v2,\text{mix}}$, and 81.4% with Ni = 30 in D_{mixed}. Moreover, in comparison to the 1&1 combination, the average percentage of the SOPs drops by ≈ 28% (±9%), ≈28.2% (±7%), and ≈26% (±2%), respectively. Additionally, the 1&10 combination exhibits a comparable behavior to the 5&5, but with a slight drop in both the average accuracy (∼1% in $D_{v1,\text{mix}}$, ≈3% in $D_{v2,\text{mix}}$, and ≈2% in D_{mixed}) and the average percentage of computational cost ≈14% (±2%) in $D_{v1,mix}$, ≈10% (±4%) in $D_{v2,\text{mix}}$, and ≈13% (±7%) in D_{mixed}).

We re-assessed the input sizes T examined in Section VI-A (employing D_{mixed}) utilizing the chosen networks to validate the persistence of the trade-off achieved in Step 1 (see Fig. 7). Fig. 13 demonstrates the evaluation results. Both RSNNs, {5&5, Ni = 30} and {1&10, Ni = 30}, exhibit a consistent trend observed in step 1 (see Fig. 8). For the former, the network exhibited a drop of 3% in accuracy and a gain of 9.3% in computational cost compared to the evaluation done with 200-ms input duration. Similarly, the latter network showed a 3.8% decrease in accuracy and a 9.9% gain in computational cost. Therefore, the trade-off achieved in step 1 persists.

2) Reducing Inference t_{steps}: After checking the validation of T_{min}, we applied the final optimization method on the selected RSNNs, {5&5, Ni = 30} and {1&10, Ni = 30}, to reduce their inference t_{steps} as described in Section IV-B.

Table V depicts the optimized number of time steps, which are considered to be sufficient during the inference to maintain the same classification accuracy. The standard deviation coupled with the time steps represents the disparity among the samples in the testing set. The proposed method succeeded in saving remarkable but varying time steps for each combination during the inference. As illustrated, and based on the adopted $T_{\min} = 150$ ms (300 time steps), the network linked to the 5&5 combination requires 220 time steps to retain the same classification accuracy, resulting in a saving rate of 26.6%. Similarly, the network associated with 1&10 requires 238 time steps, achieving a reduction rate of 20.6%. Moreover, to preserve the original classification accuracy, the proposed method was tuned with a patience value of 120 time steps for both networks.

In total, the proposed system paves the way toward a real-time hardware deployment to perform online classification with minimal use of hardware resources due to the implemented optimization methods. The future work involves deploying the selected networks on a dedicated neuromorphic device (i.e., Intel Loihi2 chip [34]) to present an end-to-end neuromorphic system for tactile texture classification, with event-based and asynchronous communication, and spike-based computing. A drawback in our approach is that the proposed system was evaluated under controlled experimental conditions, specifically utilizing known indentation force and sliding velocity values commonly found in the literature. However, it is essential to note that in real-world scenarios, these conditions are often both unknown and unstable. Therefore, another future goal is to transition the experimental data collection conditions to a more realistic environment, simulating to a certain extent, real application scenarios. Further research endeavors could focus on exploring the versatility of this neuromorphic tactile system through the investigation of diverse tactile applications. These may include tasks such as stiffness and hardness classification, and objection recognition. In light of the hard constraints required for real-time inferences in prosthetic and robotic applications, the proposed neuromorphic tactile sensing system stands as a suitable candidate for integration. A potential scenario for utilizing it can be by mapping the real-time event-driven inferences to feedback or control-based systems for rapid and efficient post-processing closed-loop scenarios, such as safe and proper interaction with the environment. Another possible scenario can be employing the spikes emitted by the modeled mechanoreceptors (SA-I and RA-I) from the raw signals of our PVDF-based sensing system in human-in-the-loop psychophysical experiments. This could be achieved by mapping the spikes or their associated features to a feedback system for the user. This would allow exploiting the frequency range of such sensing systems, in exploring the somatosensory system activity such as information encoding and decoding as done in [59].

VII. Conclusion

In this article, we presented a neuromorphic tactile sensing system designed for textural features classification. The core of our system lies in its capability to directly handle raw signals obtained from our PVDF-based sensing system. This eliminates the need for feature extraction to perform classification, thereby addressing the challenges highlighted in the literature. To achieve this, we modeled the firing dynamic of the SA-I and RA-I mechanoreceptors, encoding both transient and static information applied to the sensors, to spikes carrying spatiotemporal features. Subsequently, the emitted spikes are conveyed to an RSNN, trained using the SGD to perform inferences and classification. We proposed an optimization method to the RSNN based on tuning t_{ref} during the encoding phase, to impose a trade-off between computational cost and classification accuracy. We found that two RSNNs {5&5, Ni = 30} and {1&10, Ni = 30} achieved the best trade-off among the rest of the evaluated combinations (see Section VI-C), making them a favorable candidate for real-time deployment and inferences. Following this, we reduced the inference time steps t_{steps} of these networks through a rate-coding-based approach for further optimization. The method detects the neuron with the highest spike count in the readout layer through an adaptable patience value (see Section IV-B). The proposed method succeeded in saving 26.6% and 20.6% out of the total time steps for the {5&5, Ni = 30} and {1&10, Ni = 30} networks, respectively. The main conclusion that can be elicited from this study is the feasibility of relying on insights from neuroscience (i.e., refractory period of spiking neurons) to develop an elaboration system that fits the constraints of real-time applications. In particular, and as demonstrated in our work, the refractory period influences the spiking activity, making it an interesting parameter that can be leveraged by neuromorphic devices, which predominantly depend on spike-driven communication for inferences.

References

[1] Å. B. Vallbo and R. S. Johansson, "Properties of cutaneous mechanoreceptors in the human hand related to touch sensation," *Hum. Neurobiol.*, vol. 3, no. 1, pp. 3–14, 1984.

[2] V. E. Abraira and D. D. Ginty, "The sensory neurons of touch," *Neuron*, vol. 79, no. 4, pp. 618–639, 2013.

[3] L. Seminara et al., "A hierarchical sensorimotor control framework for human-in-the-loop robotic hands," *Sci. Robot.*, vol. 8, no. 78, May 2023, Art. no. eadd5434.

[4] Y. Abbass, S. Dosen, L. Seminara, and M. Valle, "Full-hand electrotactile feedback using electronic skin and matrix electrodes for high-bandwidth human–machine interfacing," *Phil. Trans. Roy. Soc. A, Math., Phys. Eng. Sci.*, vol. 380, no. 2228, Jul. 2022, Art. no. 20210017.

[5] R. S. Dahiya, P. Mittendorfer, M. Valle, G. Cheng, and V. J. Lumelsky, "Directions toward effective utilization of tactile skin: A review," *IEEE Sensors J.*, vol. 13, no. 11, pp. 4121–4138, Nov. 2013.

[6] A. Mazzoni et al., "Morphological neural computation restores discrimination of naturalistic textures in trans-radial amputees," *Sci. Rep.*, vol. 10, no. 1, pp. 1–14, Jan. 2020.

[7] Y. Amin, C. Gianoglio, and M. Valle, "Embedded real-time objects' hardness classification for robotic grippers," *Future Gener. Comput. Syst.*, vol. 148, pp. 211–224, Nov. 2023.

[8] M. Alameh, Y. Abbass, A. Ibrahim, and M. Valle, "Smart tactile sensing systems based on embedded CNN implementations," *Micromachines*, vol. 11, no. 1, p. 103, Jan. 2020.

[9] A. Dabbous, A. Ibrahim, M. Alameh, M. Valle, and C. Bartolozzi, "Object contact shape classification using neuromorphic spiking neural network with STDP learning," in *Proc. IEEE Int. Symp. Circuits Syst. (ISCAS)*, May 2022, pp. 1052–1056.

[10] Y. Abbass, M. Saleh, S. Dosen, and M. Valle, "Embedded electrotactile feedback system for hand prostheses using matrix electrode and electronic skin," *IEEE Trans. Biomed. Circuits Syst.*, vol. 15, no. 5, pp. 912–925, Oct. 2021.

[11] H. Fares, Y. Abbass, M. Valle, and L. Seminara, "Validation of screen-printed electronic skin based on piezoelectric polymer sensors," *Sensors*, vol. 20, no. 4, p. 1160, Feb. 2020.

[12] M. Alameh, Y. Abbass, A. Ibrahim, G. Moser, and M. Valle, "Touch modality classification using recurrent neural networks," *IEEE Sensors J.*, vol. 21, no. 8, pp. 9983–9993, Apr. 2021.

[13] U. B. Rongala, A. Mazzoni, and C. M. Oddo, "Neuromorphic artificial touch for categorization of naturalistic textures," *IEEE Trans. Neural Netw. Learn. Syst.*, vol. 28, no. 4, pp. 819–829, Apr. 2017.

[14] A. K. Gupta, A. Nakagawa-Silva, N. F. Lepora, and N. V. Thakor, "Spatio-temporal encoding improves neuromorphic tactile texture classification," *IEEE Sensors J.*, vol. 21, no. 17, pp. 19038–19046, Sep. 2021.

[15] S. Sankar et al., "Texture discrimination with a soft biomimetic finger using a flexible neuromorphic tactile sensor array that provides sensory feedback," *Soft Robot.*, vol. 8, no. 5, pp. 577–587, Oct. 2021.

[16] M. Rasouli, Y. Chen, A. Basu, S. L. Kukreja, and N. V. Thakor, "An extreme learning machine-based neuromorphic tactile sensing system for texture recognition," *IEEE Trans. Biomed. Circuits Syst.*, vol. 12, no. 2, pp. 313–325, Apr. 2018.

[17] Y. Zhengkun and Z. Yilei, "Recognizing tactile surface roughness with a biomimetic fingertip: A soft neuromorphic approach," *Neurocomputing*, vol. 244, pp. 102–111, Jun. 2017.

[18] C. Jiang, L. Yang, and Y. Zhang, "A spiking neural network with spike-timing-dependent plasticity for surface roughness analysis," *IEEE Sensors J.*, vol. 22, no. 1, pp. 438–445, Jan. 2022.

[19] L. Seminara et al., "Towards integrating intelligence in electronic skin," *Mechatronics*, vol. 34, pp. 84–94, Mar. 2016.

[20] F. E. Erukainure, V. Parque, M. A. Hassan, and A. M. R. FathEl-Bab, "Estimating the stiffness of kiwifruit based on the fusion of instantaneous tactile sensor data and machine learning schemes," *Comput. Electron. Agricult.*, vol. 201, Oct. 2022, Art. no. 107289.

[21] C. Gianoglio, E. Ragusa, P. Gastaldo, and M. Valle, "A novel learning strategy for the trade-off between accuracy and computational cost: A touch modalities classification case study," *IEEE Sensors J.*, vol. 22, no. 1, pp. 659–670, Jan. 2022.

[22] S. Barburiceanu, S. Meza, B. Orza, R. Malutan, and R. Terebes, "Convolutional neural networks for texture feature extraction. Applications to leaf disease classification in precision agriculture," *IEEE Access*, vol. 9, pp. 160085–160103, 2021.

[23] L. L. Bologna, J. Pinoteau, R. Brasselet, M. Maggiali, and A. Arleo, "Encoding/decoding of first and second order tactile afferents in a neurorobotic application," *J. Physiol.*, vol. 105, nos. 1–3, pp. 25–35, 2011.

[24] S. F. Müller-Cleve et al., "Braille letter reading: A benchmark for spatio-temporal pattern recognition on neuromorphic hardware," *Frontiers Neurosci.*, vol. 16, Nov. 2022, Art. no. 951164.

[25] C. Bartolozzi, G. Indiveri, and E. Donati, "Embodied neuromorphic intelligence," *Nature Commun.*, vol. 13, no. 1, p. 1024, Feb. 2022.

[26] M. I. Jordan, "Artificial intelligence-the revolution hasn't happened yet," *Harvard Data Sci. Rev.*, vol. 1, no. 1, pp. 1–9, 2019.

[27] A. Ibrahim and M. Valle, "Real-time embedded machine learning for tensorial tactile data processing," *IEEE Trans. Circuits Syst. I, Reg. Papers*, vol. 65, no. 11, pp. 3897–3906, Nov. 2018.

[28] G. Indiveri and S. Liu, "Memory and information processing in neuromorphic systems," *Proc. IEEE*, vol. 103, no. 8, pp. 1379–1397, Aug. 2015.

[29] C. Mead, "Neuromorphic electronic systems," *Proc. IEEE*, vol. 78, no. 10, pp. 1629–1636, Oct. 1990.

[30] E. Chicca, F. Stefanini, C. Bartolozzi, and G. Indiveri, "Neuromorphic electronic circuits for building autonomous cognitive systems," *Proc. IEEE*, vol. 102, no. 9, pp. 1367–1388, Sep. 2014.

[31] R. Douglas, "Neuromorphic analogue VLSI," *Annu. Rev. Neurosci.*, vol. 18, no. 1, pp. 255–281, Jan. 1995.

[32] S.-C. Liu and T. Delbruck, "Neuromorphic sensory systems," *Current Opinion Neurobiol.*, vol. 20, no. 3, pp. 288–295, Jun. 2010.

[33] E. Neftci, J. Binas, U. Rutishauser, E. Chicca, G. Indiveri, and R. J. Douglas, "Synthesizing cognition in neuromorphic electronic systems," *Proc. Nat. Acad. Sci. USA*, vol. 110, no. 37, pp. E3468–E3476, Sep. 2013.

[34] M. Davies et al., "Loihi: A neuromorphic manycore processor with on-chip learning," *IEEE Micro*, vol. 38, no. 1, pp. 82–99, Jan. 2018.

[35] K. H. Long, J. D. Lieber, and S. J. Bensmaia, "Texture is encoded in precise temporal spiking patterns in primate somatosensory cortex," *Nature Commun.*, vol. 13, no. 1, p. 1311, Mar. 2022.

[36] K. E. Friedl, A. R. Voelker, A. Peer, and C. Eliasmith, "Human-inspired neurorobotic system for classifying surface textures by touch," *IEEE Robot. Autom. Lett.*, vol. 1, no. 1, pp. 516–523, Jan. 2016.

[37] E. M. Izhikevich, "Which model to use for cortical spiking neurons?" *IEEE Trans. Neural Netw.*, vol. 15, no. 5, pp. 1063–1070, Sep. 2004.

[38] R. Xu, H. Akay, and S.-G. Kim, "Buckled MEMS beams for energy harvesting from low frequency vibrations," *Research*, vol. 2019, pp. 1–14, Jan. 2019.

[39] L. Seminara, M. Capurro, P. Cirillo, G. Cannata, and M. Valle, "Electromechanical characterization of piezoelectric PVDF polymer films for tactile sensors in robotics applications," *Sens. Actuators A, Phys.*, vol. 169, no. 1, pp. 49–58, Sep. 2011.

[40] E. O. Neftci, H. Mostafa, and F. Zenke, "Surrogate gradient learning in spiking neural networks: Bringing the power of gradient-based optimization to spiking neural networks," *IEEE Signal Process. Mag.*, vol. 36, no. 6, pp. 51–63, Nov. 2019.

[41] M. Saleh, Y. Abbass, A. Ibrahim, and M. Valle, "Experimental assessment of the interface electronic system for PVDF-based piezoelectric tactile sensors," *Sensors*, vol. 19, no. 20, p. 4437, Oct. 2019.

[42] T. Callier, H. P. Saal, E. C. Davis-Berg, and S. J. Bensmaia, "Kinematics of unconstrained tactile texture exploration," *J. Neurophysiol.*, vol. 113, no. 7, pp. 3013–3020, Apr. 2015.

[43] B. Rostamian et al., "Texture recognition based on multi-sensory integration of proprioceptive and tactile signals," *Sci. Rep.*, vol. 12, no. 1, p. 21690, Dec. 2022.

[44] A. I. Weber et al., "Spatial and temporal codes mediate the tactile perception of natural textures," *Proc. Nat. Acad. Sci. USA*, vol. 110, no. 42, pp. 17107–17112, Oct. 2013.

[45] W. Gerstner, W. M. Kistler, R. Naud, and L. Paninski, *Neuronal Dynamics: From Single Neurons to Networks and Models of Cognition*. Cambridge, U.K.: Cambridge Univ. Press, 2014.

[46] E. M. Izhikevich, "Simple model of spiking neurons," *IEEE Trans. Neural Netw.*, vol. 14, no. 6, pp. 1569–1572, Nov. 2003.

[47] P. Dayan and L. F. Abbott, *Theoretical Neuroscience: Computational and Mathematical Modeling of Neural Systems*. Cambridge, MA, USA: MIT Press, 2005.

[48] A. Sahasranamam, I. Vlachos, A. Aertsen, and A. Kumar, "Dynamical state of the network determines the efficacy of single neuron properties in shaping the network activity," *Sci. Rep.*, vol. 6, no. 1, p. 26029, 2016.

[49] S. S. Kim, A. P. Sripati, R. J. Vogelstein, R. S. Armiger, A. F. Russell, and S. J. Bensmaia, "Conveying tactile feedback in sensorized hand neuroprostheses using a biofidelic model of mechanotransduction," *IEEE Trans. Biomed. Circuits Syst.*, vol. 3, no. 6, pp. 398–404, Dec. 2009.

[50] F. Zenke and T. P. Vogels, "The remarkable robustness of surrogate gradient learning for instilling complex function in spiking neural networks," *Neural Comput.*, vol. 33, no. 4, pp. 899–925, Mar. 2021.

[51] J. K. Eshraghian et al., "Training spiking neural networks using lessons from deep learning," 2021, *arXiv:2109.12894*.

[52] M. Sadek Bouanane, D. Cherifi, E. Chicca, and L. Khacef, "Impact of spiking neurons leakages and network recurrences on event-based spatio-temporal pattern recognition," 2022, *arXiv:2211.07761*.

[53] Y. LeCun, Y. Bengio, and G. Hinton, "Deep learning," *Nature*, vol. 521, no. 7553, pp. 436–444, May 2015.

[54] Microsoft. (2021). *Neural Network Intelligence*. [Online]. Available: https://github.com/microsoft/nni

[55] M. Sorbaro, Q. Liu, M. Bortone, and S. Sheik, "Optimizing the energy consumption of spiking neural networks for neuromorphic applications," *Frontiers Neurosci.*, vol. 14, p. 662, Jun. 2020.

[56] M. Berry and M. Meister, "Refractoriness and neural precision," in *Proc. Adv. Neural Inf. Process. Syst.*, vol. 10, 1997, pp. 2200–2211.

[57] F. Gabbiani and S. J. Cox, "Quantification of spike train variability," in *Mathematics for Neuroscientists*, F. Gabbiani and S. J. Cox, Eds. London, U.K.: Academic, 2010, pp. 237–249. [Online]. Available: https://www.sciencedirect.com/science/article/pii/B9780123748829000150

[58] C. Gianoglio, E. Ragusa, P. Gastaldo, and M. Valle, "Trade-off between accuracy and computational cost with neural architecture search: A novel strategy for tactile sensing design," *IEEE Sensors Lett.*, vol. 7, no. 5, pp. 1–4, May 2023.

[59] C. M. Oddo et al., "Artificial spatiotemporal touch inputs reveal complementary decoding in neocortical neurons," *Sci. Rep.*, vol. 7, no. 1, p. 45898, 2017.

Haydar Al Haj Ali received the B.S. and M.Sc. degrees in biomedical engineering from the Lebanese International University, Lebanon, in 2019 and 2021, respectively. He is currently pursuing the Ph.D. degree in science and technology for electronic and telecommunication engineering with the Department of Naval, Electrical, Electronic, and Telecommunications Engineering (DITEN), University of Genoa, Genoa, Italy.

His research interests include embedded neuromorphic computing, machine learning for resource-constrained devices, signal processing, and tactile sensing systems for biomedical applications.

Yahya Abbass (Member, IEEE) received the B.S. degree in electronics and the M.Sc. degree in signal, telcom, speech, and image from the Faculty of Science, Lebanese University, Beirut, Lebanon, in 2016 and 2018, respectively, and the Ph.D. degree from the Department of Electric, Electronic, Telecommunication Engineering and Naval Architecture (Connected Objects, Smart Materials, Integrated Circuits—COSMIC Laboratory), University of Genoa, Genoa, Italy, in 2021.

Until 2023, he was a Postdoctoral Researcher with the Department of Electric, Electronic, Telecommunication Engineering and Naval Architecture (Connected Objects, Smart Materials, Integrated Circuits—COSMIC Laboratory), University of Genoa, where he has been a Research Fellow since 2023. His research interests include biomedical circuits and systems, electronic or artificial sensitive skin, tactile sensing systems for prosthetics and robotics, and electronic and microelectronic systems.

Christian Gianoglio (Member, IEEE) received the master's degree in electronic engineering and the Ph.D. degree in electrical engineering from the University of Genoa, Genoa, Italy, in 2015 and 2018, respectively.

He is currently a Research Fellow with the Department of Naval, Electrical, Electronic, and Telecommunications Engineering (DITEN), University of Genoa. His research interests include machine learning for resource-constrained devices and real-time applications, signal processing and machine learning for tactile sensing systems, and pattern recognition for quality assessment of insulation systems in electrical apparatuses.

Ali Ibrahim (Member, IEEE) received the M.S. degree in industrial control from the Doctoral School of Sciences and Technologies, Lebanese University, Beirut, Lebanon, in 2009, and the dual Ph.D. (Hons.) degrees in electronic and computer engineering and robotics and telecommunications from the University of Genoa, Genoa, Italy, and Lebanese University in 2016.

He was a Postdoctoral Researcher with the Department of Electric, Electronic, Telecommunication Engineering and Naval Architecture, University of Genoa, from 2016 to 2018. He is currently an Assistant Professor with the Department of Electrical and Electronics Engineering, Lebanese International University, Beirut, and an Associate Researcher with the Department of Electric, Electronic, Telecommunication Engineering and Naval Architecture, University of Genoa. He has more than 70 publications in journals and international conferences. His research interests involve embedded and tiny machine learning, FPGA implementation, interface electronics for electronic skin systems, approximate computing, and techniques and methods for energy-efficient embedded computing.

Changjae Oh (Member, IEEE) received the B.S., M.S., and Ph.D. degrees in electrical and electronic engineering from Yonsei University, Seoul, South Korea, in 2011, 2013, and 2018, respectively.

From 2018 to 2019, he was a Postdoctoral Research Assistant at the Queen Mary University of London, London, U.K., where he is a Lecturer at the School of Electronic Engineering and Computer Science and the Centre for Intelligent Sensing.

Maurizio Valle (Senior Member, IEEE) received the M.S. degree in electronic engineering and the Ph.D. degree in electronics and computer science from the University of Genoa, Genoa, Italy, in 1985 and 1990, respectively.

Since December 2019, he has been a Full Professor of Electronics with the Department of Naval, Electrical, Electronic, and Telecommunications Engineering (DITEN), University of Genoa, where he leads the Connected Objects, Smart Materials, Integrated Circuits Laboratory. He has been and is in charge of many research contracts and projects funded at local, national, and European levels and by Italian and foreign companies. His research interests include biomedical circuits and systems, electronic/artificial sensitive skin, tactile sensing systems for prosthetics and robotics, neuromorphic touch sensors, and electronic and microelectronic systems.

Open Access funding provided by 'Università degli Studi di Genova' within the CRUI CARE Agreement